



**HAL**  
open science

# Investigation of dielectric layers laser ablation mechanism on n-PERT silicon solar cells for (Ni) plating process: Laser impact on surface morphology, composition, electrical properties and metallization quality

Cécile Molto, Jung Eun Lee, Jan Nekarda, Varun Arya, Solène Béchu, Muriel Bouttemy, Arnaud Etcheberry, Etienne Drahi, Pierre-Philippe Grand, Anne-Marie Goncalves

## ► To cite this version:

Cécile Molto, Jung Eun Lee, Jan Nekarda, Varun Arya, Solène Béchu, et al.. Investigation of dielectric layers laser ablation mechanism on n-PERT silicon solar cells for (Ni) plating process: Laser impact on surface morphology, composition, electrical properties and metallization quality. *Solar Energy Materials and Solar Cells*, 2019, 202, pp.110149. 10.1016/j.solmat.2019.110149 . hal-03119383

**HAL Id: hal-03119383**

**<https://hal.science/hal-03119383>**

Submitted on 20 Jul 2022

**HAL** is a multi-disciplinary open access archive for the deposit and dissemination of scientific research documents, whether they are published or not. The documents may come from teaching and research institutions in France or abroad, or from public or private research centers.

L'archive ouverte pluridisciplinaire **HAL**, est destinée au dépôt et à la diffusion de documents scientifiques de niveau recherche, publiés ou non, émanant des établissements d'enseignement et de recherche français ou étrangers, des laboratoires publics ou privés.



Distributed under a Creative Commons Attribution - NonCommercial 4.0 International License

# Investigation of dielectric layers laser ablation mechanism on n-PERT silicon solar cells for (Ni) plating process: laser impact on surface morphology, composition, electrical properties and metallization quality.

Cécile Molto<sup>a,b,c</sup>, Jung Eun Lee<sup>b</sup>, Jan Nekarda<sup>d</sup>, Varun Arya<sup>d</sup>, Solène Bechu<sup>b,c</sup>, Muriel Bouttemy<sup>c</sup>, Arnaud Etcheberry<sup>c</sup>, Etienne Drahi<sup>b,c</sup>, Pierre-Philippe Grand<sup>a,b</sup>, Anne-Marie Goncalves<sup>c</sup>

<sup>a</sup>EDF R&D, IPVF, 18 avenue Thomas Gobert, 91120 Palaiseau, France

<sup>b</sup>Institut Photovoltaïque d'Ile-de-France (IPVF), 18 avenue Thomas Gobert, 91120 Palaiseau, France

<sup>c</sup>Institut Lavoisier de Versailles (ILV), Université de Versailles Saint-Quentin-en-Yvelines, Université Paris-Saclay, 45 avenue des États-Unis, 78035 Versailles, France

<sup>d</sup>Fraunhofer Institute for Solar Energy Systems ISE, Heidenhofstrasse 2, 79110 Freiburg im Breisgau, Germany

<sup>e</sup>TOTAL GRP-New Energies, Tour Coupole 32ème étage, 2 Place Jean Millier--La Défense 6, 92078 Paris La Défense Cedex

## ABSTRACT

Laser contact opening is a critical step for solar cells manufacturing and needs to be optimized to achieve high efficiencies. In this paper, laser contact opening using a picosecond laser (wavelength 355 nm, pulse duration 10 ps) has been carried out on n-PERT precursors composed of a  $\text{SiO}_x/\text{SiO}_x\text{N}_y$  stack on the rear polished side and a  $\text{SiO}_x\text{N}_y$  layer on the front textured side. By varying peak fluence from 0.130 J/cm<sup>2</sup> to 2.159 J/cm<sup>2</sup> and spot overlapping, ninety parameters combinations have been tested to open these dielectric layers. Surface morphology characterization, before and after laser ablation, has been realized using Confocal Laser Scanning Microscopy and Scanning Electron Microscopy. Bulk and surface compositions have also been investigated by Energy Dispersive Spectroscopy and X-ray Photoelectron Spectroscopy analysis, respectively. Results have shown the existence of four separated laser impacted areas on the polished side and a related ablation mechanism is suggested. Also, electrical characterization using four probe measurements and calibrated lifetime photoluminescence revealed that electrical properties of the silicon underlying increased when post laser annealing was performed associated with no spot overlapping. Then, nickel electroless deposition has been performed and first characterizations indicate adherence issues and inhomogeneous metallization. Characterization of metallized samples revealed that these observations were closely linked to the non-homogenous surface morphology and composition after laser ablation.

**Keywords:** n-PERT cell, UV-picosecond laser, ablation mechanism, surface damages, Ni plating

## 1. Introduction

There is no doubt that it is critical to develop renewable energies to meet future energy demand and limit global warming. In this context, researchers and industrials aim to make solar technology more and more

efficient and cost effective. For Si-wafer based photovoltaic (PV) technology, which accounted for about 95 % of the total solar PV production in 2018 [1], metallization step is of critical interest. Nowadays, screen printing (SP) is the leading metallization technology to produce industrial silicon solar cells as it is simple, fast and suitable for mass production. However, this method relies on silver (Ag) and/or aluminum (Al) containing pastes, which are the most process critical and most expensive non silicon material used in current crystalline silicon (c-Si) cells according to the last International Technology Roadmap for Photovoltaic (ITRPV) [1]. Calculations based on this roadmap evidence the need to considerably reduce silver consumption to develop a sustainable PV technology at the multi-TeraWatt level. Indeed, silver consumption varies from 100 to 270 mg/cell depending on the cell concept which represents 3.6 to 9.7 g/module (36 cells/module). In the last three years, around 100 GW PV capacities have been installed per year, corresponding to 317.46 million additional modules if we consider a production of 315 W/module. On this basis, PV industry requires 1142 to 3079 tons of silver/year so 4.66 to 12.58% of annual silver production (24468 tons of silver production in 2018 [2]). Considering a scenario where PV contributes to a 100% renewable energy-based power sector (ITRPV scenario 3), the objective would be to achieve 10 TW of PV capacity within 2035. That represents an increase of around 600 GW per year so a consumption of 28 to 75 % of the silver produced per year. Moreover, SP has almost reached its limitations in term of contact quality and different ways to apply metallic contacts are required for high efficient cell architectures and advanced cell concepts [3]. Alternative metallization techniques are, as a result, under investigation such as SP derivatives (inkjet, stencil, aerosol printing ...) or electrochemical metallization also called “plating”. A combination of two alternatives metallization techniques is also interesting as shown by Gerdes et al., where a molten solder ( $\text{Sn}_{96}\text{Ag}_3\text{Cu}$ ) is printed on an electroplated Ni/Ag seed layer (Starjet technology) for front side metallization [4].

In this study, Ni/Cu plating was used as metallization technique which not only gives a solution to metal cost reduction by using cheaper metals but also has the potential to overcome SP limitations (more dense contacts, higher conductivity, better aspect ratio, narrower line width, lower contact resistance) [5]. A first step to selectively open the dielectric layers is necessary before electrochemical metallization. The most widely used technique is laser ablation as it enables high throughputs and can be reliably integrated into production lines [6]. Furthermore, this technique is a very accurate contactless method, not relying on chemical products which reduces risks of breakage and contamination.

Non-optimized laser parameters can lead to inefficient dielectric layers removal, underlying silicon surface melting, silicon amorphization, micro-cracks and/or defects formation. Laser induced damages on silicon solar cells and their impacts on the cell performances have already been studied [7–16]. It has been demonstrated that laser induced damages can provide a sink for copper diffusion which means that the optimization of laser parameters is crucial to ensure reliability of Ni/Cu plated silicon solar cells [17]. Dang et al. [18] have investigated the reliability of plated Ni/Cu/Ag stacks for c-Si solar cells. They have demonstrated lower efficiency and faster degradation with thermal ageing, by using high power laser ablation due to higher dislocations density induced by laser ablation. Likewise, copper diffusion has been observed after thermal ageing at 235°C and was found to be more important with high power laser ablation. Optimization of dielectric layer laser opening is not only crucial to achieve high efficient silicon solar cells, but also to ensure the reliability of metallized contacts.

Working principle of laser ablation is described in literature [19–21]. Ablation mechanism depends on laser source (ultra-violet (UV), green or infrared (IR)), pulse duration (femtosecond (fs), picosecond (ps) or nanosecond (ns) scale) and material properties (band gap and reflectivity). If laser beam energy is higher than the material band gap, absorption occurs while a laser beam with an energy lower than the material band gap will not be absorbed, except in specific conditions. For instance, at high optical intensity, it is possible to bridge the band gap by simultaneous absorption of two or more lower-energy photons, where the sum of photons energies exceeds the material band gap. This is a non-linear optical phenomenon called multi-photon absorption that more likely happen in case of ultra-short or short laser pulses combined with high intensity laser pulses [11]. The time scale for electron cooling and energy transfer to the lattice is in the order of ps. Consequently, with very short pulse duration (femtosecond laser) a high quantity of excited electrons will transfer their energy to the lattice (non-radiative electron-phonon transfer) in a very short time scale. The lattice is heated at a picosecond scale and matter is directly sublimated which enables to neglect thermal conduction into the rest of the sample [19]. Thus, ultra-short laser pulses are potentially more suitable to reduce laser induced damages by limiting thermal impact into silicon under dielectric layers [22,23]. Moreover, UV laser radiations create laser induced defects with a shallower spatial distribution [23,24] which is better for silicon solar cells. Heinrich et al. have particularly worked on SiN<sub>x</sub> dielectric layer ablation on silicon solar cells and described three main ablation mechanisms: lift-off, partial lift-off and direct ablation [10,11,16]. The modifications of laser source, pulse duration or dielectric layers properties can completely change ablation mechanism and the determination of most suitable laser source and processing parameters is still not clearly identified.

In this work, we study the ablation mechanism using UV-ps (pulse duration 10 ps) on n-PERT (Passivated Emitter Rear Totally diffused) silicon solar cells having SiO<sub>x</sub>N<sub>y</sub>/SiO<sub>x</sub> passivation stack on the rear polished side and SiO<sub>x</sub>N<sub>y</sub> on the front textured side. The choice of laser source and pulse duration was motivated by 3 reasons: 1) Optical penetration depth is smaller with UV laser radiations than with green and infrared ones so spatial distribution of defects is shallower [23]; 2) femtosecond lasers are still too expensive while nanosecond lasers cause too high thermal impact. Picosecond lasers still limit thermal impact which reduces damages and provides lower opening width; 3) Short laser pulses, as picosecond, demonstrate formation of laser induced periodic surface structures (LIPSS) making silicon surface rougher which is beneficial for adhesion of plated contacts [17]. Thus, laser induced damages on the morphology, composition and electrical properties of silicon after ablation have been investigated. Palladium (Pd) activation of the silicon surface followed by Ni electroless deposition is then realized to investigate impact of laser damages on the metallization process.

## **2. Experimental details**

### *2.1. Materials*

All experiments were carried out on large area (156 x 156 mm<sup>2</sup>) 180 μm-thick monocrystalline n-PERT silicon solar cells precursors from ISC Konstanz (Fig. 1). These precursors contain a 500 nm thick emitter with a sheet resistance of approximately 85 Ω/sq, a base resistivity of 1 Ω.cm and a 500 nm thick phosphorus doped area on rear side with a sheet resistance of about 80 Ω/sq. The front side is textured with random pyramids and a 70 nm thick silicon oxide nitride layer is deposited by Plasma Enhanced Chemical Vapor Deposition (PECVD) for passivation and antireflection properties (refractive index = 2.03). The rear side is polished and a PECVD

oxide-nitride stack is deposited. Silicon oxide ( $\text{SiO}_x$ ) is approximately 10 nm thick and silicon oxide nitride ( $\text{SiO}_x\text{N}_y$ ) is 70 nm thick.

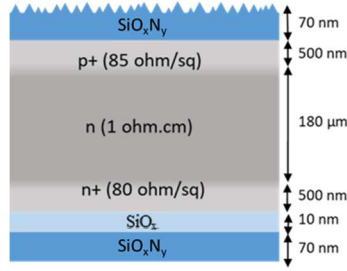


**Fig. 1.** Representation of n-PERT precursor cell structure

Dielectric layers have been opened in air atmosphere using a UV-ps laser (HyperRapid laser from Coherent with a Gaussian beam profile having 20  $\mu\text{m}$  diameter ( $1/e^2$ ), pulse duration is 10 ps and frequency is 400 kHz). Part of precursors has been opened on the front side and another part on the rear side to study each side separately. Several laser ablations have been performed by varying the peak fluence ( $F_{\text{peak}}$ ) in the range of 0.130  $\text{J}/\text{cm}^2$  to 2.159  $\text{J}/\text{cm}^2$  and the distance between two centers of lasered spots ( $d$ ) from 4  $\mu\text{m}$  to 36  $\mu\text{m}$  to test various overlapping conditions. Patterns are designed with a CAO software as shown in Fig. 2. to obtain ninety parameter combinations.

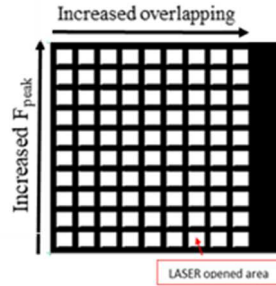


**Fig. 2.** Patterns used for dielectric layer laser opening on n-PERT precursors.  $F_{\text{peak}}$ : 0.130  $\text{J}/\text{cm}^2$ , 0.269  $\text{J}/\text{cm}^2$ , 0.448  $\text{J}/\text{cm}^2$ , 0.505  $\text{J}/\text{cm}^2$ , 0.668  $\text{J}/\text{cm}^2$ , 0.766  $\text{J}/\text{cm}^2$ , 0.896  $\text{J}/\text{cm}^2$ , 1.385  $\text{J}/\text{cm}^2$ , 1.809  $\text{J}/\text{cm}^2$ , 2.159  $\text{J}/\text{cm}^2$  from bottom to top. Distance between two centers spot  $d = 4 \mu\text{m}$ , 8  $\mu\text{m}$ , 12  $\mu\text{m}$ , 16  $\mu\text{m}$ , 20  $\mu\text{m}$ , 24  $\mu\text{m}$ , 28  $\mu\text{m}$ , 32  $\mu\text{m}$ , 36  $\mu\text{m}$  from left to right.

A short post laser annealing (PLA) is then performed at 750°C (30 seconds temperature build up followed by cooling) under  $\text{N}_2$  using a Jipelec Jetfirst furnace from Semco technology. This step must be performed before plating to provide hydrogen diffusion. In principle, hydrogen diffusion is realized during final firing when SP metallization at around 800°C is used. In our case, Ni/Cu metallization stack cannot undergo such annealing temperatures that is why plating process requires an additional annealing step. PLA parameters have been optimized in a previous work to achieve the best carrier lifetimes. PLA is followed by immersion in an activation solution containing HF 1% and Pd ions to deoxidize and activate the silicon surface before Ni electroless deposition.

## 2.2. Characterization methods

Process steps and characterization methods employed are described in Fig. 3. Characterization highlights laser induced damages and allows understanding ablation mechanism to further optimize laser parameters.

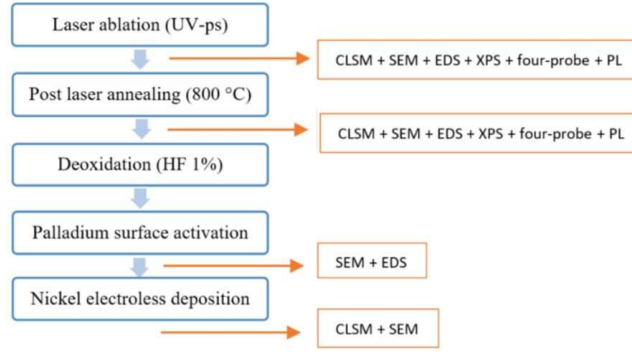


**Fig. 3.** Description of metallization process steps and characterizations pathway.

Confocal Laser Scanning Microscopy (CLSM) is used to investigate surface morphology with LEXT OLS 5000 equipment from Olympus. In addition, images are realized with Scanning Electron Microscopy (SEM) (Zeiss Merlin VP compact) at 15 keV as operating voltage and 3.8 mm working distance. Chemical bulk composition is investigated by Energy Dispersive Spectroscopy (EDS) analysis at the same voltage and 10.5 mm working distance and Bruker silicon Drift Detectors. X-ray Photoelectron Spectroscopy (XPS) surface chemical analyses are carried out with a Thermo Electron K-Alpha<sup>+</sup> spectrometer using a monochromatic Al-K $\alpha$  X-Ray source (1486.6 eV). The Thermo Electron K-Alpha<sup>+</sup> spectrometer procedure is used to calibrate the spectrometer and verified using Cu and Au samples following the ASTM-E-902-94 standard procedure. Acquisition parameters of high energy resolution photo peaks are: 400  $\mu$ m spot size, 12 kV primary energy, 6.0 mA emission intensity, Constant Analyser Energy mode (CAE) 10 eV and 0.05 eV energy step size. Data are processed using the Thermo Fisher scientific Avantage<sup>©</sup> data system with the sensitivity factors of AlThermo1 library. The background is calculated using the Shirley method. The peaks modeling is performed using Gaussian/Lorentzian mix (30%). The electronic quality of underlying silicon is studied by four-probe measurements and  $\tau_{\text{eff}}$  is determined by quasi steady state photo conductance calibrated at high magnification photoluminescence (PL QSS-PC using a RS2 from BTImaging) using an injection level of  $1\text{E}^{15}$ . Reflectivity value is necessary for PL QSS-PC measurements and have been determined for each sample by reflectivity measurements using UV-Vis-NIR spectrophotometer Carry 5000 from Agilent. The refractive index (n) and the optical band gap of the  $\text{SiO}_y\text{N}_x$  layer are determined on the rear side by ellipsometry using Uvisel2 equipment from Horiba and a Tauc law for signal extrapolation  $\text{SiO}_x\text{N}_y$ .

### 3. Results and discussion

#### 3.1. Morphology and composition of ablated precursors

##### 3.1.1. Study on the rear polished side

We first characterized samples with CLSM after laser ablation on the rear polished side to get rid of topography and facilitate the interpretation. As shown in optical and laser intensity images represented in Fig. 4, the surface morphology depends on  $F_{\text{peak}}$  used. Both optical and laser intensity images are displayed because they give complementary information. Typically, on laser intensity images, surface appears in dark grey when the dielectric layers are removed.

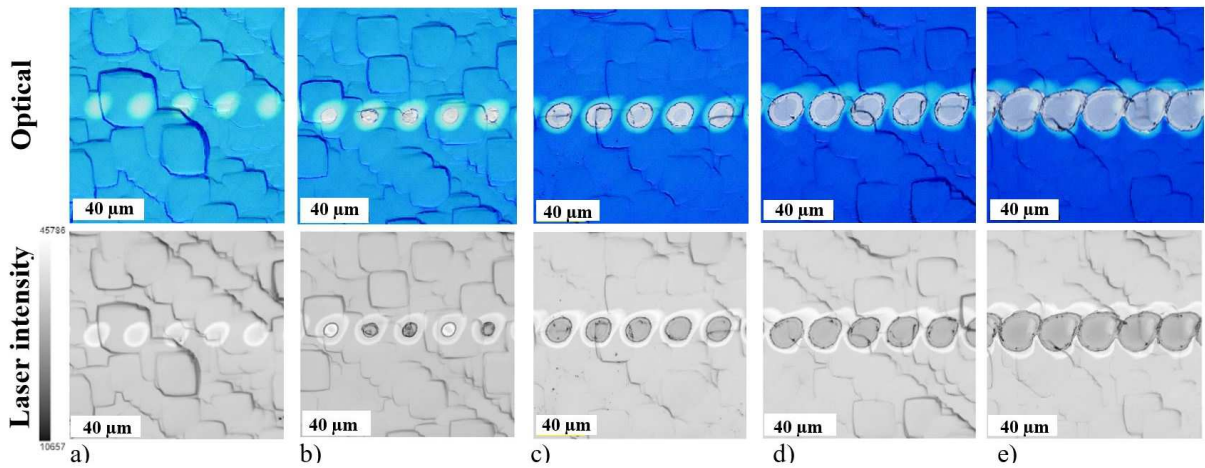


**Fig. 4.** CLSM images on rear polished side after laser ablation using  $d = 24 \mu\text{m}$  and various  $F_{\text{peak}}$  a)  $0.130 \text{ J/cm}^2$  b)  $0.269 \text{ J/cm}^2$  c)  $0.505 \text{ J/cm}^2$  d)  $0.896 \text{ J/cm}^2$  e)  $2.159 \text{ J/cm}^2$ . Top images correspond to images recorded through optical excitation and bottom one through laser excitation (405 nm).

$F_{\text{peak}} = 0.130 \text{ J/cm}^2$  is not sufficient to remove the dielectric layers (Fig. 4.a)) but surface is still impacted as observed with the appearance of light blue areas. By increasing the  $F_{\text{peak}}$  to  $0.269 \text{ J/cm}^2$ , the dielectric layers start to be removed in some areas (Fig.4.b)) so the fluence threshold ( $F_{\text{th}}$ ) is close to  $0.269 \text{ J/cm}^2$ . At  $F_{\text{peak}} = 0.505 \text{ J/cm}^2$  and over (Fig.4.c)), the dielectric layers are well removed and three different areas can be discriminated. These areas are illustrated in Fig. 5.a) and named to facilitate further explanations. Given the Gaussian shape of the laser beam, these three areas have not received the same photons quantity:

- Area n°1: inner spot. This area, at the laser beam center, receives more photons and is the most impacted.
- Area n°2: opened spot. This is the entire part where the dielectric layers are removed. This area includes the inner spot and an area around it which is less impacted due to lower quantity of photons received.
- Area n°3: light blue area. This part is affected but not ablated and is called heat-affected zone (HAZ). This morphology has already been observed in literature and corresponds to amorphous silicon under dielectric layers [10,17,25]. Laser parameters do not enable energy absorption by the dielectric layers in this area but underlying silicon can absorb it. As a result, silicon is locally melted and the fast cooling prevents silicon recrystallization leading to amorphous silicon (a-Si) formation. The width of light blue area decreases when  $F_{\text{peak}}$  increases due to Gaussian shape of the laser beam.

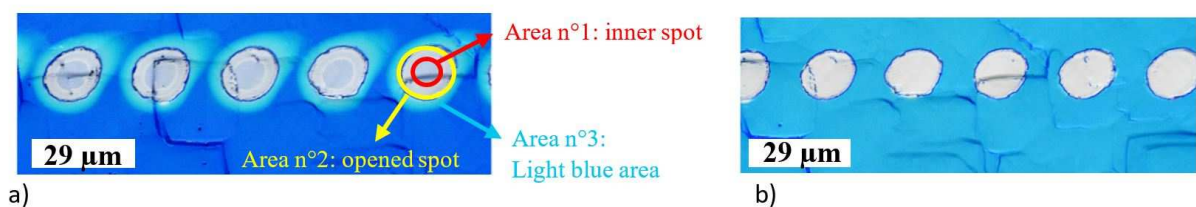


**Fig. 5.** CLSM optical images representing the different surface morphologies after laser ablation ( $d = 24 \mu\text{m}$ ,  $F_{\text{peak}} = 0.505 \text{ J/cm}^2$  a) before PLA b) after PLA

After post-laser annealing at 750 °C (Fig.5.b)), the light blue area completely disappears for all laser parameters tested in this study. This supports the hypothesis of an amorphous silicon formation in this region. Indeed, PLA allows silicon to recrystallize as a-Si starts to crystallize at 640°C [26]. Area n°1 is much less visible after PLA but does not completely disappear (visible on laser intensity images not shown here).

Now, if we take into account laser spot overlapping, area n°3 is still visible but areas n°1 and 2 progressively give a way to double impacted areas (Fig. 6). As observed in Fig.6.a) and b), the laser ablation is not efficient enough with low  $F_{\text{peak}}$  (0.269 J/cm<sup>2</sup>) as the entire layer is not removed. Overlapping is thus necessary to supply more energy to the sample and provide dielectric layers removal (Fig 6. c) and d)). On the one hand, overlapping can promote ablation for low fluences but, on the other hand, overlapped areas are potentially more damaged when higher  $F_{\text{peak}}$  (for instance  $F_{\text{peak}} = 0.505$  J/cm<sup>2</sup> in Fig 6. e)) are used.

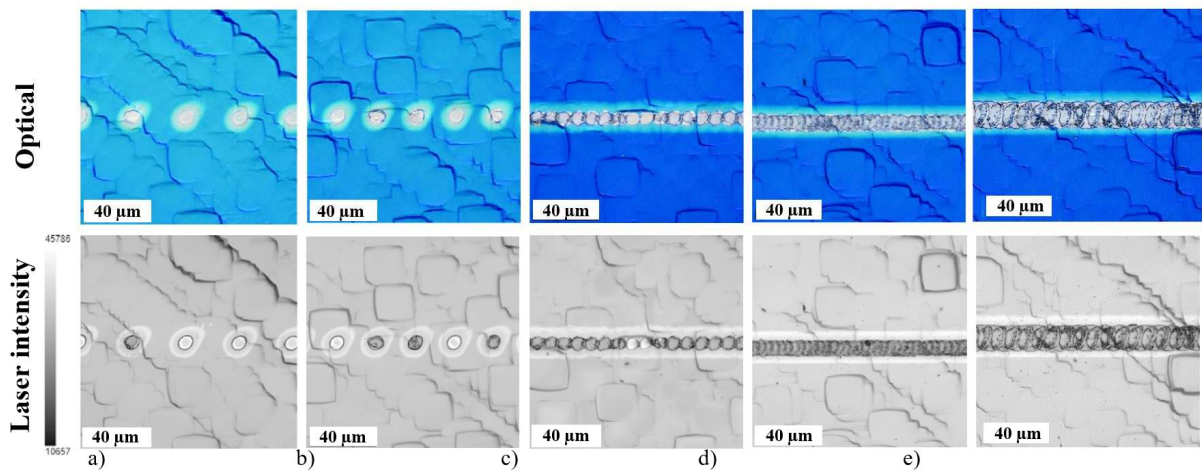


**Fig. 6.** CLSM images on the rear polished side after laser ablation a)  $F_{\text{peak}}$  of 0.269 J/cm<sup>2</sup>,  $d = 32$  μm, b)  $F_{\text{peak}}$  of 0.269 J/cm<sup>2</sup>,  $d = 24$  μm, c)  $F_{\text{peak}}$  of 0.269 J/cm<sup>2</sup>,  $d = 8$  μm, d)  $F_{\text{peak}}$  of 0.269 J/cm<sup>2</sup>,  $d = 4$  μm e)  $F_{\text{peak}}$  of 0.505 J/cm<sup>2</sup>,  $d = 8$  μm. Top images correspond to images recorded through optical excitation and bottom one through laser excitation (405 nm).

In order to investigate in more details the surface morphology after laser ablation, we used SEM to characterize samples on the rear side and two sets of conditions are shown in Fig. 7:  $F_{\text{peak}} = 0.505$  J/cm<sup>2</sup>,  $d = 12$  μm and  $F_{\text{peak}} = 1.809$  J/cm<sup>2</sup> and  $d = 24$  μm. As the Si crystallinity differences are not detectable through SEM measurements, we cannot distinguish the previous light blue area (area n°3) observed in CLSM pictures, but areas n°1 and 2 are clearly visible. Consequently, pictures before and after PLA appear similar with SEM characterization. Higher magnification results allow us to see a thin external corona in addition to the previous areas observed thanks to CLSM pictures and described above and will be named area n°2<sub>bis</sub>. By looking at laser spot edges, the dielectric layers seem to have been lifted off from the silicon surface and sharp residues are sometimes visible close to opening areas. On double impacted areas and area n°2<sub>bis</sub>, a very specific surface morphology is appearing, which is already described in literature, and called LASER-induced periodic surface structures (LIPSS) [7,14,15,17]. The generally accepted explanation of these structures is an interference between the incident light and a surface wave generated by scattering. This interference leads to periodic modulation of the absorbed intensity and consequently to modulated ablation. As shown later, LIPSS are more likely present on the textured front side.

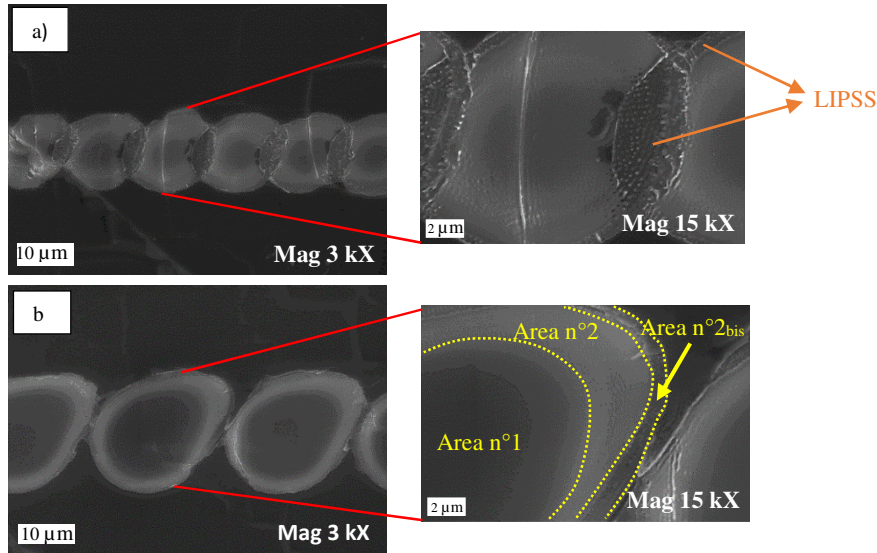


**Fig. 7.** SEM images after laser ablation on the rear polished side a)  $F_{\text{peak}} = 0.505 \text{ J/cm}^2$ ,  $d = 12 \text{ }\mu\text{m}$ , b)  $F_{\text{peak}} = 1.809 \text{ J/cm}^2$ ,  $d = 24 \text{ }\mu\text{m}$

The overall composition has been determined by EDS measurements evidencing the presence of Si, O and C but not N. However, as EDS measurements are not enough surface sensitive, the presence of N cannot be excluded due to the detection limit of the technique (micrometric interaction volume). We performed complementary XPS measurements before and after PLA, in order to obtain the surface composition and more information about the fine chemistry evolution after LASER opening. As the XPS spot size is about  $400 \text{ }\mu\text{m}$ , it is then impossible to obtain separated information on the different areas defined before in the tenth of micrometer dimension. Only double impacted areas were then investigated by analyzing sample with 50 % overlapping of opened areas to maximize the contribution of open areas to the global measurement. Fig 8. b) and c) show XPS analysis results for Si2p and O1s photopeaks after laser ablation using  $F_{\text{peak}} = 1.809 \text{ J/cm}^2$  and  $d = 12 \text{ }\mu\text{m}$ .

From the survey spectra (not shown here), four elements (as expected) were detected: silicon, oxygen, nitrogen, and carbon. Carbon presence (7.2 at.%) is attributed to sample inherent superficial contamination. The Si2p spectrum (Fig 8 c)) shows two main environments, the first one, at 98.5 eV (Si2p<sub>3/2</sub> contribution), is attributed to the crystalline Si wafer [27], the second one, at 103.5 eV fitted using only one contribution, corresponds to oxide phases [28] in agreement with O1s predominant oxide contribution at 532.7 eV. A minor suboxide phase at 100.9 eV is also detected as well as a very low SiO<sub>x</sub>N<sub>y</sub> oxynitride contribution at 105.2 eV. This is coherent with the low signal levels of O1s contribution at 534.4 eV and N1s photopeak, visible by using XPS contrarily to EDS, and presenting a specific double structure assigned to the oxynitride organization [29]. The last O contribution at 532.0 eV corresponds to the O involved in the C contamination layer. The detection of the Si substrate signal indicates that the oxidized layer is either inhomogeneous, or presents a thickness inferior to about 10 nm (photoelectron escape depth). This signal brings also information about the atomic arrangement. Indeed, the spin-orbit splitting is not as outlined as the one expected for a crystalline Si, the Si2p<sub>3/2</sub> and Si2p<sub>1/2</sub> contributions being larger (1.00 eV vs 0.40 eV expected). It suggests a disorganization of the atomic network, whose main probable origin is the interaction with laser, leading to amorphization.

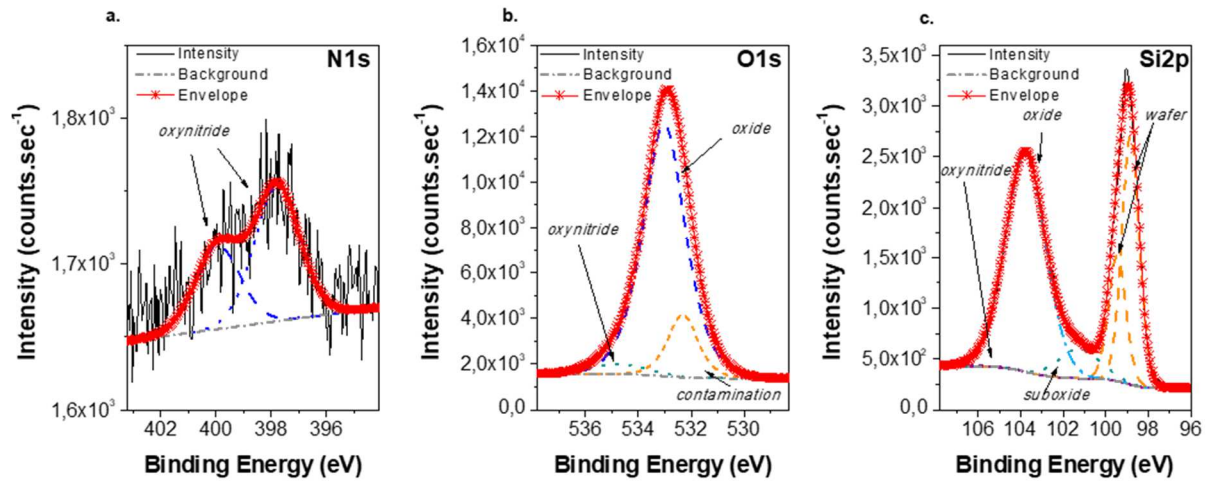


**Fig. 8.** High energy resolution XPS spectra of N1s (a.), O1s (b.) and Si2p (c.) after laser ablation at  $F_{\text{peak}} = 1.809 \text{ J/cm}^2$  and  $d = 12 \mu\text{m}$  (50 % overlapping).

Similar photopeak reconstructions are obtained for all the fluences studied, but with a variability of the different contributions proportion and stoichiometry, as evidenced on the Fig 9. presenting the superimposition of the Si2p regions and in Table 1. Indeed, the qualitative comparison of Si2p peak envelopes shows that a  $\text{SiO}_x\text{N}_y$  contribution is present for 0.269 and 0.448  $\text{J/cm}^2$  and becomes negligible compared to the oxide and substrate ones at higher fluences.

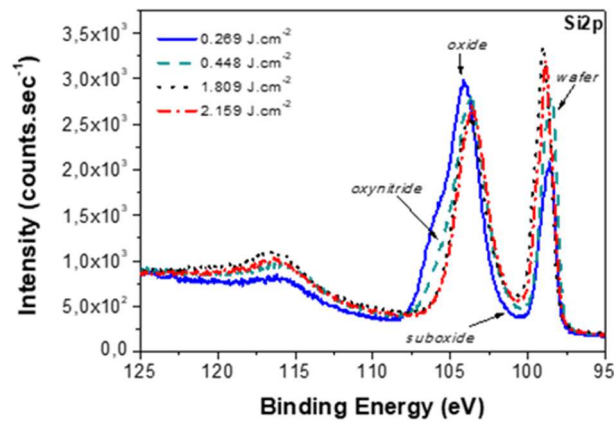


**Fig 9.** High resolution XPS spectra of Si2p after laser ablation for different fluences.

**Table 1.** Stoichiometry obtained after reconstruction of the XPS spectra for the different  $F_{\text{peak}}$  studied for  $\text{SiO}_x$  and  $\text{SiO}_x\text{N}_y$  environments. \*few accuracy due to the low oxynitride environment presence.

	$F_{\text{peak}} \text{ (J/cm}^2\text{)}$	<b>0.269</b>	<b>0.448</b>	<b>1.809</b>	<b>2.159</b>
$\text{SiO}_x$	<b>O/Si</b>	0.98	1.45	1.68	1.51
	<b>(O+N)/Si</b>	2.12	1.86	30.00*	59.00*
$\text{SiO}_x\text{N}_y$	<b>(O/N)</b>	1.48	1.67	2.33	4.90

To get more insight on laser ablation effect at the surface, a closer study of the  $\text{SiO}_x$  and  $\text{SiO}_x\text{N}_y$  stoichiometry is presented in Table 1. As observed, the O/Si ratios corresponding to the  $\text{SiO}_x$  environment rise

with  $F_{\text{peak}}$  from 0.98 to 1.68, which is lower than expected. Indeed, the deposition of  $\text{SiO}_x$  layer by PECVD aims to obtain silicon oxide layer close to thermal silicon oxide and  $\text{O/Si}$  ratio is commonly superior to 1.5 [30]. One hypothesis is that the silicon oxide observed in double impacted areas is a consequence of the laser process. After ablation of  $\text{SiO}_x\text{N}_y/\text{SiO}_x$  initial stack, we can suppose that silicon substrate becomes more reactive to oxygen, due to the laser heating phenomenon for example, which could explain the  $\text{O/Si}$  ratio increasing with  $F_{\text{peak}}$ . Consequently, it is also impossible to attest that a complete  $\text{SiO}_x$  elimination had been performed.

Concerning the  $\text{SiO}_x\text{N}_y$  environment, the oxynitride contribution decreases with the laser fluence with a threshold at  $F_{\text{peak}} = 1.809 \text{ J/cm}^2$  from which this contribution becomes practically negligible. Consequently, only ratios determined at  $F_{\text{peak}} = 0.269$  and  $0.448 \text{ J/cm}^2$  will be considered. Not only the  $(\text{O}+\text{N})/\text{Si}$  but also the  $\text{O/N}$  ratios vary with  $F_{\text{peak}}$ , in opposite trends (decrease and increase respectively).

From these observations, we can conclude that higher fluences allow to completely remove the  $\text{SiO}_x\text{N}_y$  layer while lower fluences lead to surfaces presenting lower quality. These differences can probably be due to a lack of overlapping issues between spot lines as seen in Fig 10.

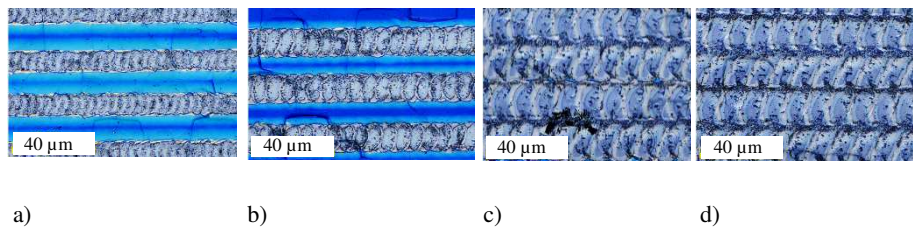


**Fig 10.** CLSM optical images of laser opened samples (50% overlapping) analyzed by XPS. a)  $F_{\text{peak}}$  of  $0.269 \text{ J/cm}^2$  b)  $F_{\text{peak}}$  of  $0.448 \text{ J/cm}^2$  c)  $F_{\text{peak}}$  of  $1.809 \text{ J/cm}^2$  d)  $F_{\text{peak}}$  of  $2.159 \text{ J/cm}^2$

XPS analyses have also been carried out after PLA and revealed that  $\text{Si}2p_{3/2}$  peak contribution (attributed to the crystalline Si wafer) was shifted towards higher energies and started to recover its spin orbit splitting (Fig. 11 b). It becomes more similar to the peak corresponding to a purely crystalline silicon wafer represented in Fig. 11 a). This is consistent with the hypothesis of a-Si recrystallization after PLA. However, it is clear that silicon crystallinity is better but not completely recovered. It would be interesting in a further work to investigate different PLA conditions to achieve a complete silicon crystallinity recovering.

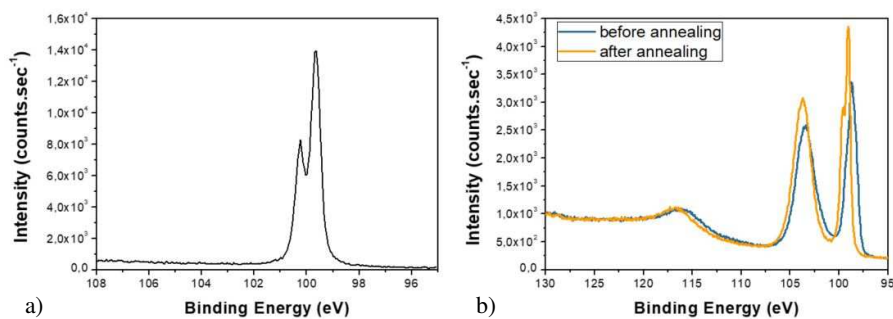


**Fig 11.** High resolution XPS spectra of  $\text{Si}2p$  a) for a crystalline silicon wafer b) after laser ablation on precursors using  $F_{\text{peak}}$  of  $1.809 \text{ J/cm}^2$  and 50% overlapping followed by a post laser annealing

To fully investigate the ablation mechanism, it is necessary to consider properties of dielectric layers on the rear side. At 300K, the band gap of silicon is 1.12 eV [31] and according to Chen et al. [32] the optical band gap

of silicon oxide deposited by PECVD is around 3-4 eV depending on the deposition parameters (Tauc plot determination method). We have calculated the band gap of  $\text{SiO}_x\text{N}_y$  on the rear polished side by ellipsometry. We have plotted  $(\alpha hv)^{1/r} = f(hv)$  to obtain a Tauc diagram,  $\alpha$  representing the absorption coefficient,  $h$  the Planck constant,  $\nu$  the frequency and  $r$  is equal to 1/2 for a direct band gap and 2 for an indirect band gap. Therefore, we obtain a band gap of 3.6 eV for  $\text{SiO}_x\text{N}_y$  layer. In UV, photons have an energy of 3.49 eV so we can consider that direct energy absorption is possible in underlying silicon but multiphotonic process is required for absorption in silicon oxide and silicon oxynitride. Based on these considerations and previous characterization results, we propose an ablation mechanism based on partial lift-off represented in Fig. 12.

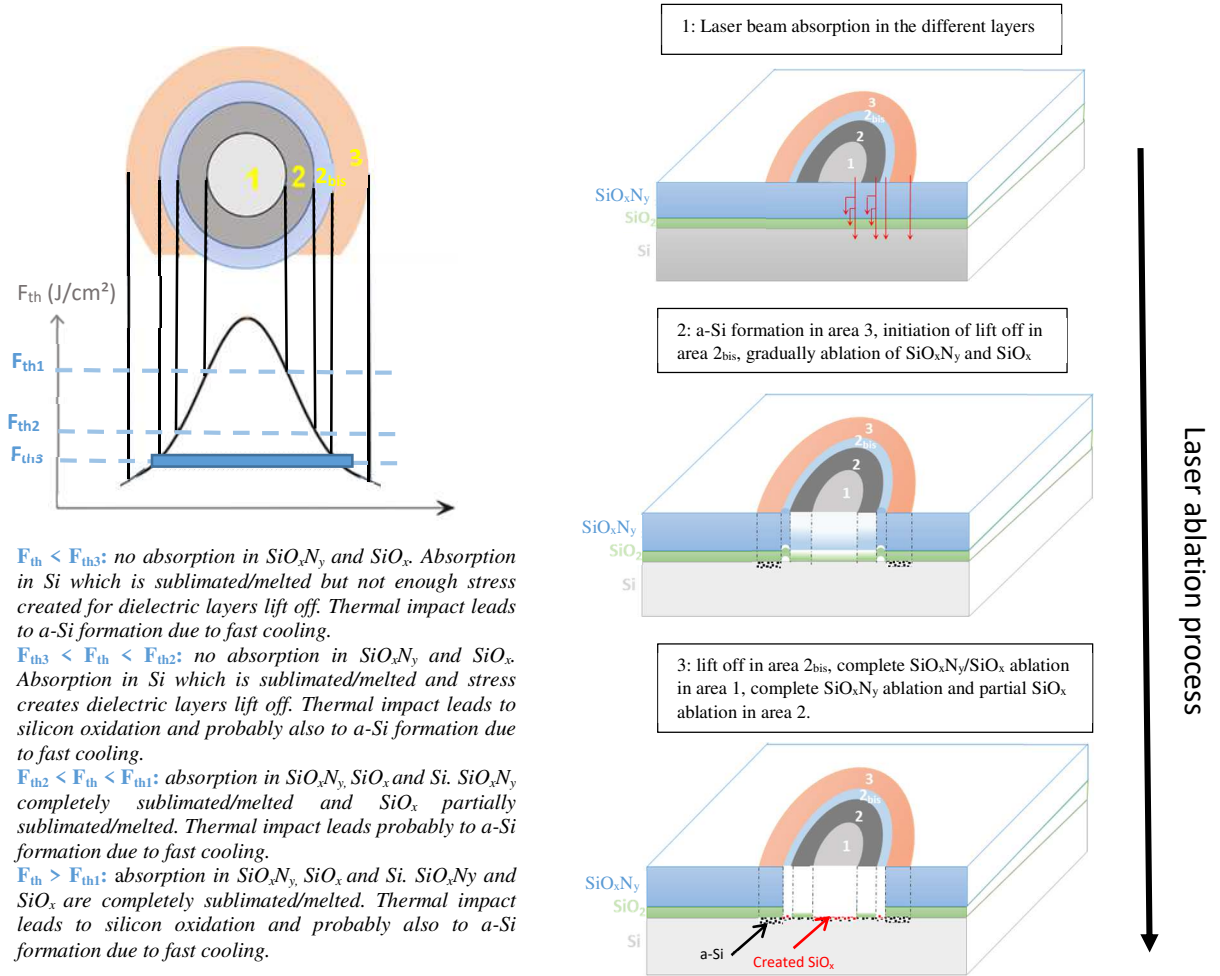


**Fig. 12.** Proposed ablation mechanism based on partial lift-off of  $\text{SiO}_x\text{N}_y/\text{SiO}_x$  passivation stack on the rear polished side with UV-ps laser.

Laser pulse duration is 10 ps, which enables to bring high quantity of photons in a short time. In these conditions, matter thermalization is low and ablation can occur through sublimation without passing by melting and liquid phases.

- In area n°1 and n°2, fluence is high enough to promote multiabsorption in silicon oxynitride and silicon oxide. Firstly, energy is absorbed in silicon oxynitride, which is sublimated. If the fluence is high enough, a part of energy is absorbed by silicon underlying and silicon oxide.  $\text{SiO}_x$  is sublimated too but silicon can be reoxidized through surface heating.

However, if the fluence is not high enough to completely sublimate silicon oxide, this generates a gradient along the laser spot where silicon oxide is thicker at the edge of area n°2. The contrast observed in SEM could be due to the different thicknesses of remaining SiO<sub>x</sub>.

- In area n°2<sub>bis</sub>, silicon oxynitride and silicon oxide hardly absorbed the laser energy because there are not enough photons to promote multiphotonic absorption. Underlying silicon absorbs this energy and is melted, creating a mechanical stress inside the dielectric layers, which are lifted off the surface. Reoxidation can occur but slowly because the fluence is low in this area.
- In area n°3, fluence is below fluence threshold. Only silicon absorbs the laser energy but melting does not create enough stress to lift off the dielectric layers above. During fast cooling, silicon is not recrystallized and amorphous silicon is formed.

In case of overlapping, morphology observed with SEM indicates that silicon surface is more thermalized (melted aspect) and XPS results suggest a-Si and SiO<sub>x</sub> formation. The probable scenario is as following:

- 1) The first impact leads to the morphology described in Fig. 12
- 2) As dielectric layers have been removed from silicon surface, all energy of the second impact is absorbed by the silicon. Moreover, silicon surface amorphization during the first impact implies the creation of intermediates energy states in silicon bandgap and so more electron-phonon transition possibilities. The second impact leads consequently to silicon surface melting and evaporation of the remaining PECVD SiO<sub>x</sub>. As the laser ablation is performed under air atmosphere we cannot avoid formation of a thin SiO<sub>x</sub> layer.

### 3.1.2. Study on the front textured side

CLSM images of the front textured side after laser ablation are shown in Fig. 13.

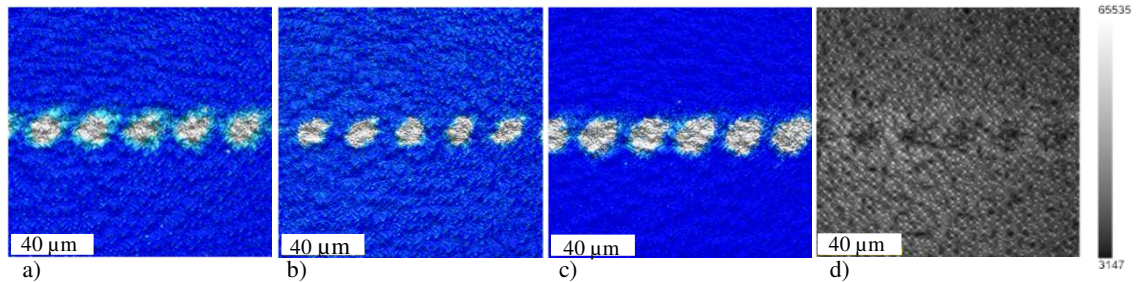


**Fig. 13.** CLSM images on the front textured side after laser ablation. a)  $F_{\text{peak}} = 0.448 \text{ J/cm}^2$ ,  $d = 24 \mu\text{m}$ , before PLA b)  $F_{\text{peak}} = 0.448 \text{ J/cm}^2$ ,  $d = 24 \mu\text{m}$ , after PLA c)  $F_{\text{peak}} = 0.896 \text{ J/cm}^2$ ,  $d = 24 \mu\text{m}$ , before PLA d)  $F_{\text{peak}} = 0.896 \text{ J/cm}^2$ ,  $d = 24 \mu\text{m}$ , before PLA. a) to c) images correspond to images recorded through optical excitation and d) one through laser excitation (405 nm).

Like for the rear polished side,  $F_{\text{peak}} = 0.130 \text{ J/cm}^2$  is not sufficient to ablate dielectric layer. The light blue area is also visible and disappears after PLA (Fig. 13. a) and b)). As observed on the rear side, the width of the light blue area decreases with  $F_{\text{peak}}$  which is clearly visible by comparing Fig. 13. a) and c). We can distinguish in Fig. 13. d) that pyramids are more impacted at high  $F_{\text{peak}}$  but textured surface makes difficult laser opened area analysis by CLSM. More accurate analysis is thus performed by SEM.

Some SEM images after laser ablation on the front side are represented in Fig. 14. Due to texturing, diffusion mechanisms occur but differently on the side, edges, base and top of pyramids. Consequently, ablation

mechanism is performed preferentially on edges, base and top of pyramids and residues are visible on pyramids sides (Fig. 14. a)). LIPSS structures are clearly increasing the surface roughness (Fig. 14. c)). These observations are coherent with the ones reported by Schutz-Kuchly et al. [33] in a previous study concerning UV and IR laser induced ablation of  $\text{Al}_2\text{O}_3/\text{SiN:H}$  and  $\text{a-Si:H/SiN}$ . According to Knor et al [34], interferences of laser beam with its reflection from the opposite slopes of the adjacent pyramids can explain these structures. Without overlapping, pyramids start to be highly damaged (especially the little ones) at  $F_{\text{peak}} > 0.766 \text{ J/cm}^2$ . Moreover, as shown in Fig. 14. b), even at low fluence, overlapping highly damages silicon, as top of pyramids is melted. On the one hand, more energy impacts the surface due to texturing, on the other hand, the surface is impacted several times due to overlapping. As a result, the thermal impact becomes more important explaining these observations.

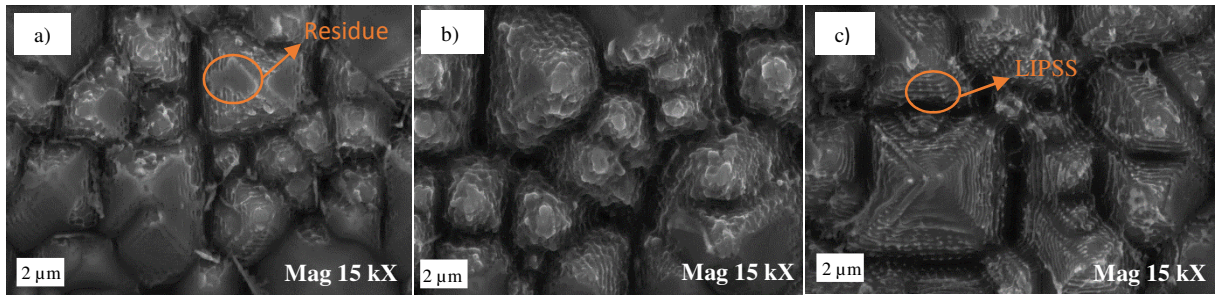


**Fig. 14.** SEM images on the front textured side after laser ablation. a)  $F_{\text{peak}} = 0.505 \text{ J/cm}^2$ ,  $d = 12 \mu\text{m}$  (no overlapping) b)  $F_{\text{peak}} = 0.505 \text{ J/cm}^2$ ,  $d = 4 \mu\text{m}$  (overlapping) c)  $F_{\text{peak}} = 1.809 \text{ J/cm}^2$ ,  $d = 24 \mu\text{m}$  (no overlapping).

XPS analyses have also been performed on the front side but texturing due to pyramids leads to difficult interpretations.  $\text{SiO}_x\text{N}_y$  contribution is globally more important on the front side compared to the rear side, suggesting a higher proportion of dielectric layer residues, as visible in Fig. 14 a). Similarly to the rear side,  $\text{Si}2p_{3/2}$  peak contribution is shifted toward lower energy and a spin orbit loss is noted, suggesting the presence of  $\text{a-Si}$  after laser ablation. However, no significant modifications are observed after PLA.

Ellipsometry measurements are not suitable for textured surface, so we will assume similar band gap values of the  $\text{SiO}_x\text{N}_y$  layer on both sides. As there is no silicon oxide layer,  $\text{SiO}_x\text{N}_y$  absorbs energy and is sublimated, but meanwhile, silicon underlying is melted and  $\text{SiO}_x\text{N}_y$  is lifted off. Ablation mechanism on the front side is also based on partial lift-off.

### 3.2. Impact of laser ablation on electrical properties

Four-probe measurements have been realized on the ninety patterns before and after PLA. The measurements are realized in the center of  $1 \times 1 \text{ cm}^2$  ablated squares and under dark. On the  $p^+$  front side, resistance square ( $R_{\text{sq}}$ ) should be equal to  $85 \Omega/\text{sq}$  if the silicon surface is not damaged after laser ablation. On the  $n^+$  rear side the  $R_{\text{sq}}$  should be equal to  $80 \Omega/\text{sq}$  but as the bulk is also n-type, the measure will take into account the bulk as follow:  $R_{\text{sq}} = (R_{\text{sq,totale}} \times R_{\text{sq,bulk}}) / (R_{\text{sq,bulk}} - R_{\text{sq,totale}})$  with  $R_{\text{sq,bulk}} = \rho_{\text{bulk}} / e_{\text{bulk}} = 1 / 0.018 = 55.55 \Omega$ .

With  $\rho_{\text{bulk}}$ , the resistivity of the bulk ( $\rho_{\text{bulk}} = 1 \Omega\cdot\text{cm}$ ), and  $e_{\text{bulk}}$ , the thickness of the bulk ( $e_{\text{bulk}} = 0.0180 \text{ cm}$ ). If the silicon is not damaged during laser ablation,  $R_{\text{sq}}$  should be equal to  $80 \Omega/\text{sq}$  and the  $R_{\text{sq,totale}}$  measured should

be equal to:  $R_{sq,totale} = (R_{sq,bulk} \times R_{sq}) / (R_{sq,bulk} + R_{sq}) = (55.55 \times 80) / (55.55 + 80) = 32.78 \text{ } \Omega/\text{sq}$ . On Fig. 15, results at extreme cases are represented:

- $R_{sq}$  evolution after laser ablation using highest  $F_{peak} = 2.159 \text{ J/cm}^2$  and various distances  $d$  are shown in Fig. 15.a)). CLSM images have been used to determine the distance at which the laser beam starts to overlap. We clearly see that  $R_{sq}$  largely depends on laser beam overlapping. As long as there is no overlapping,  $R_{sq}$  stays close to its initial value (90  $\Omega/\text{sq}$  on the front side and 32.78  $\Omega/\text{sq}$  on the rear side) even at the highest  $F_{peak}$  tested. It confirms that thermal effect is low with ps laser and that damaged surface is shallow when UV wavelength is used. In addition, the detrimental effect of overlapping is confirmed as the more the overlapping is, the higher the  $R_{sq}$  is. This evolution can be due to 1) defects formation (dislocations, cracks...) caused by multiple impacts on the surface, 2) doping profile modification under thermal effect induced by overlapping. Further investigations using other characterization techniques such as Deep Level Transient Spectroscopy and Secondary Ion Mass Spectroscopy would be necessary to completely understand these results. The front side is more sensitive to overlapping because textured surface leads to diffused beam energy which impacts several times the surface. As a result, the  $R_{sq}$  achieves values up to 300  $\Omega$ . At  $d = 4 \text{ } \mu\text{m}$  on the front side, the  $R_{sq}$  abruptly decreases to 32-33  $\Omega/\text{sq}$ . Here, damages are so deep that n/p+ junction is broken and we actually measure the  $R_{sq}$  of n/n+ stack, as for the rear side.
- $R_{sq}$  evolution using lowest distance  $d = 4 \text{ } \mu\text{m}$  and various  $F_{peak}$  are shown in Fig. 15.b). Here the surface undergoes multiple laser impacts. As expected, with high fluence the junction p+/n on the front side is destroyed as  $R_{sq}$  drastically decreases to 32-33  $\Omega/\text{sq}$ . However, electrical properties are not impacted provided that lowest  $F_{peak} = 0.269 \text{ J/cm}^2$  is used.

In amorphous materials, localized states are present below the conduction band and above the valence band mobility edges as a consequence of lattice disorder. Thus, geminate recombinations are more likely to occur and carrier mobility is much lower. By promoting a-Si recrystallization, PLA reduces recombination and therefore  $R_{sq}$  value, as seen in Fig. 15. Four probe measurements revealed that overlapping must be preferably avoided, especially on the front side except for low fluence, such as  $F_{peak} = 0.269 \text{ J/cm}^2$  where no impact on electrical properties is detected.

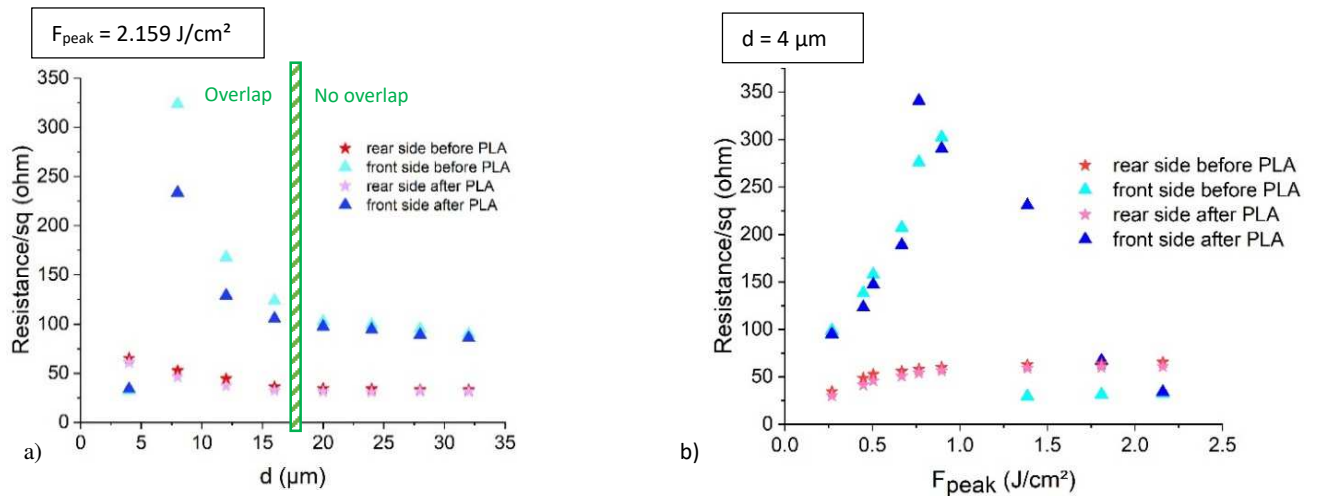


**Fig. 15.** Four-probe measurements on the rear and front side before and after PLA. a)  $F_{\text{peak}}$  of 2.159 J/cm<sup>2</sup>, variation of overlapping b)  $d = 4 \mu\text{m}$  (double or more impacted surfaces) and variation of  $F_{\text{peak}}$ .

PL QSS-PC measurements have also been carried out to investigate laser impact on the carrier lifetime. For this purpose, we decided to use another pattern to test different laser opening conditions (Fig. 16). The number of tested conditions is reduced to increase the square size and facilitate PL QSS-PC image analysis. Table 2 describes the thirty laser parameters used. For this study, it is important to precise that we define spot overlapping considering the light blue area (HAZ) and not only the opened area. Examples are given next to Table 2 for clarity. Pattern numbers in orange indicate that laser opened areas are not in contact (dielectric layers remaining). Due to the heat affected area (light blue area), dielectric layers remain between opened lines. To achieve laser contact opening where opened areas are just in contact along a line but also from one line to another, laser parameters must be adjusted. These conditions have been used for patterns underlined in green in the Table 2.

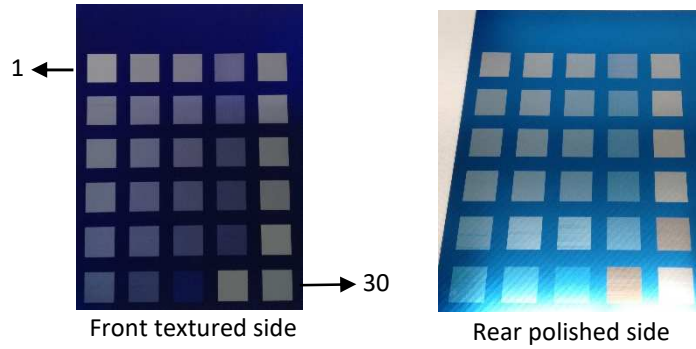
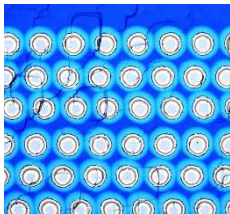


**Fig. 16.** Picture of ablated samples using various fluence and overlapping (only one side is opened for each sample). Pattern 28 on the front side and patterns 26, 27, 28 on the rear side are heat impacted but not opened.

**Table 2:** Laser ablation parameters used for PL-QSS PC characterization and 3 examples of corresponding CLSM image: overlapping percentage takes into account the light blue area.

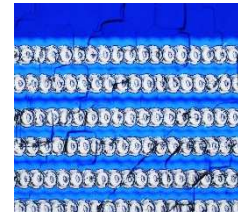
<b>1</b> 1.75 J/cm <sup>2</sup> - 75%	<b>2</b> 1.75 J/cm <sup>2</sup> - 50%	<b>3</b> 1.75 J/cm <sup>2</sup> - 25%	<b>4</b> 1.75 J/cm <sup>2</sup> - 0%	<b>5</b> 1.75 J/cm <sup>2</sup> - 25%
<b>6</b> 0.72 J/cm <sup>2</sup> - 75%	<b>7</b> 0.72 J/cm <sup>2</sup> - 50%	<b>8</b> 0.72 J/cm <sup>2</sup> - 25%	<b>9</b> 0.72 J/cm <sup>2</sup> - 0%	<b>10</b> 0.72 J/cm <sup>2</sup> - 25%
<b>11</b> 0.56 J/cm <sup>2</sup> - 75%	<b>12</b> 0.56 J/cm <sup>2</sup> - 50%	<b>13</b> 0.56 J/cm <sup>2</sup> - 25%	<b>14</b> 0.56 J/cm <sup>2</sup> - 0%	<b>15</b> 0.56 J/cm <sup>2</sup> - 25%
<b>16</b> 0.40 J/cm <sup>2</sup> - 75%	<b>17</b> 0.40 J/cm <sup>2</sup> - 50%	<b>18</b> 0.40 J/cm <sup>2</sup> - 25%	<b>19</b> 0.40 J/cm <sup>2</sup> - 0%	<b>20</b> 0.40 J/cm <sup>2</sup> - 25%
<b>21</b> 0.32 J/cm <sup>2</sup> - 75%	<b>22</b> 0.32 J/cm <sup>2</sup> - 50%	<b>23</b> 0.32 J/cm <sup>2</sup> - 25%	<b>24</b> 0.32 J/cm <sup>2</sup> - 0%	<b>25</b> 0.32 J/cm <sup>2</sup> - 25%
<b>26</b> 0.24 J/cm <sup>2</sup> - 75%	<b>27</b> 0.24 J/cm <sup>2</sup> - 50%	<b>28</b> 0.24 J/cm <sup>2</sup> - 0%	<b>29</b> 0.24 J/cm <sup>2</sup> - 75%	<b>30</b> 0.24 J/cm <sup>2</sup> - 50%



Pattern 9: opened areas not in contact



Pattern 10: opened areas in contact along a line and from one line to another



Pattern 12: overlapping of opened areas

To remove the contribution of recombination at bare silicon surface, samples are then re-passivated with amorphous silicon. 40 nm of a-Si are deposited by PECVD at 175°C using an SiH<sub>4</sub> and H<sub>2</sub> gas mixture in Octopus II tool from Indeotec. Prior to a-Si deposition, a HF cleaning is performed (HF 5 % 15 seconds) to remove silicon oxide. The surface reflectivity is an important parameter to take into account for PL QSS-PC measurements and is highly modified after a-Si deposition. Consequently, sample reflectivity after deposition have been determined with UV-Vis-NIR spectrophotometer. PL QSS-PC analysis results are illustrated in Fig. 17.

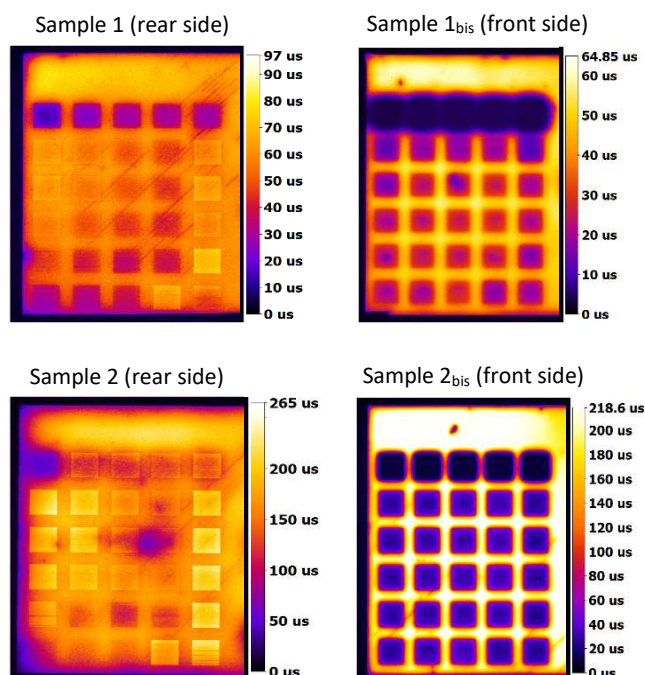


**Fig. 17.** PL QSS-PC pictures of samples a) re-passivated directly after laser ablation b) re-passivated after laser ablation and PLA.

Samples 1 and 1<sub>bis</sub> have been re-passivated directly after laser ablation while samples 2 and 2<sub>bis</sub> underwent a post laser annealing (750°C) before a-Si deposition. Differences between samples 1/1<sub>bis</sub> and 2/2<sub>bis</sub> can be mainly attributed to PLA effect.

- Laser impact on the rear side's carrier lifetime:

We observe that carrier lifetimes are almost three times higher for sample 2 where a PLA has been performed. This is consistent as there are less recombination centers when silicon crystallinity increases. That confirms the importance of PLA to recrystallize, at least partially, a-Si formed during laser ablation. For patterns underlined in green in Table 2, improvement of carrier lifetimes can be only due to a-Si recrystallization as there are no more passivation layers. For all other patterns, effect of hydrogen diffusion from remaining passivation layer to silicon can also have a beneficial effect on carrier lifetime. For patterns 1 to 5, carrier lifetimes are lower than 100 μs even after PLA and pattern 1 (75 % overlapping) is clearly the most impacted. It suggests that high fluence induces not only silicon amorphization but also defects formation (cracks, dislocations...) which are more important when the surface is impacted several times.

Patterns having few passivation layers thanks to overlapping (6, 7, 11, 12, 16, 17, 21) or no more passivation layers (patterns in green in Table 2 except pattern 5) have better carrier lifetimes. Actually, lower values are obtained with patterns presenting remaining passivation layers (patterns numbered in orange in Table 2). This trend is visible for both samples 1 and 2 but is more significant after PLA. To understand this result, we have to remind that a fluoride treatment was performed before re-passivation. Fluoride treatment etches silicon oxide from the surface and probably also a part of damaged silicon surface (silicon where crystallinity is modified), which is beneficial for carrier lifetime. For patterns where few or no passivation layer is remaining, all the laser damaged silicon surface is etched by fluoride treatment and carrier lifetimes up to 200  $\mu\text{s}$  are obtained. Adversely, remaining passivation layers hinder damaged silicon in HAZ and beneficial effect of HF treatment is lost.

- Laser impact on front side's carrier lifetime:

Textured front side is still more complicated to characterize. Carrier lifetimes are much lower than for the rear side and no significant differences are observed between various laser parameters (except for pattern 1 to 5 where high fluence is used leading to the worst carrier lifetimes). Four probe measurements allow to affirm that the p/n junction is not shunted for all laser parameters tested here. In addition, no significant improvements are visible after PLA. However, we could not have proven a-Si recrystallization after PLA on the front side with XPS results. Front side is thus more sensitive to laser ablation and there are likely more defects (cracks, dislocations) on this side. Surface texturation also leads to more important laser impact due to diffusion mechanisms but one can ask whether the doping type has an influence. Four probe measurements do not demonstrate significant impact on  $R_{sq}$  at all fluences tested showing that there is no overlapping. In contrast, PL-QSS PC results suggests an important impact on carrier lifetime, even at low fluence without overlapping.

### 3.3. Impact of laser ablation on Ni plating

A first insight of laser impact on metallization is reported here. Surface morphology after palladium and nickel deposition is investigated mainly on the rear polished side. A complete study for both sides will be the subject of a further publication including electrical characterization of metallized samples using various laser ablation parameters (I-V analysis, contact resistance measurements ...).

#### 3.3.1. Palladium deposition

SEM characterization has been performed on ablated samples after Pd activation on the rear side (Fig. 18). White particles correspond to palladium as confirmed by EDS analysis. It appears that Pd particles distribution is not homogeneous and varies with the localization in the area n°1, n°2 and n°2<sub>bis</sub> described in Fig. 12.

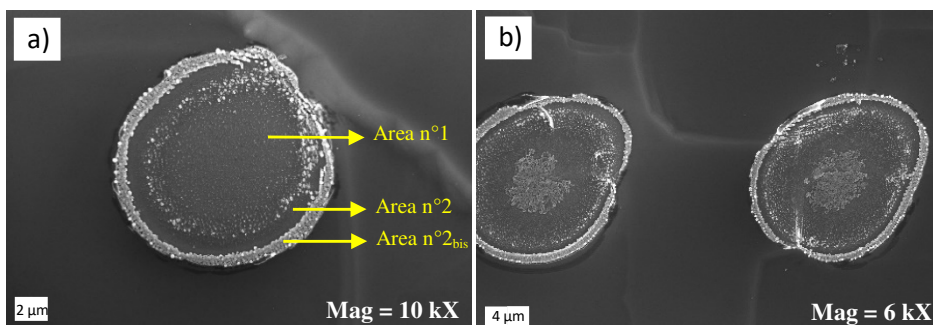


**Fig. 18.** SEM images on the rear polished side after palladium activation using different laser parameters. a)  $F_{\text{peak}}$  of 0.505 J/cm<sup>2</sup>,  $d = 28 \mu\text{m}$  b)  $F_{\text{peak}}$  of 0.896 J/cm<sup>2</sup>,  $d = 32 \mu\text{m}$ .

In the previous 3.1.1 paragraph, XPS results have demonstrated that SiO<sub>x</sub>N<sub>y</sub> layer could be removed by laser ablation using optimized conditions. However, oxides are generally still present at the ablated surface especially without spot overlapping. Palladium deposition requires the removal of potential silicon oxide present on the surface because palladium displacement deposition can only occur on bare silicon. That is why the activation solution contain hydrofluoric acid to promote silicon oxide etching [35]. Pd deposition thus depends on the surface composition (SiO<sub>x</sub> presence) but surface morphology is also important to consider as roughness will be beneficial for Pd deposition (hook points with lower surface energy). The morphology observed can be explained as follow:

- In area n°2<sub>bis</sub>, there is a high number of Pd particles. Due to lift off ablation mechanism, we have seen that silicon oxide was completely removed from the surface with low reoxidation rate. The short fluoride treatment seems sufficient to remove this thin oxide from the surface. Furthermore, roughness observed in this area favors Pd deposition.
- In area n°2, remaining silicon oxide at the surface prevents Pd deposition. As a result, a longer activation treatment or a prior immersion in HF solution would be necessary to completely remove silicon oxide and enable Pd deposition.
- In area n°1, the thinner silicon oxide is removed from the surface during activation treatment and Pd particles can be deposited. We have shown that by increasing  $F_{\text{peak}}$ , silicon oxide was thinner in area n°1 which explain the higher particles number visible in Fig. 18 b).

Furthermore, it appears that double impacted areas are uniformly metallized (not shown here), which is the consequence of roughness and thin silicon oxide. The laser ablation mechanism we have proposed in the section 3.1.1 is in good agreement with the morphology after Pd activation.

### 3.3.2. *Nickel electroless deposition*

After nickel electroless deposition, an important border effect is visible on CLSM images (Fig. 19. a)). Nickel layer is about 300 nm thicker in the border zone, which can be explained by the higher number of palladium particles in this region, enhancing the Ni plating. Pd is known as a promoting agent to nickel deposition [36,37]. Accordingly, in our configuration, nickel metallization is not homogeneous. Adherence issues are therefore visible, especially on the rear side. In particular, at high fluence ( $> 0.766 \text{ J/cm}^2$ ), the nickel deposited in the laser beam center delaminates (Fig. 19. b)). On the front side, such phenomenon is not observed as textured surface is beneficial for adherence (pyramids + LIPSS).

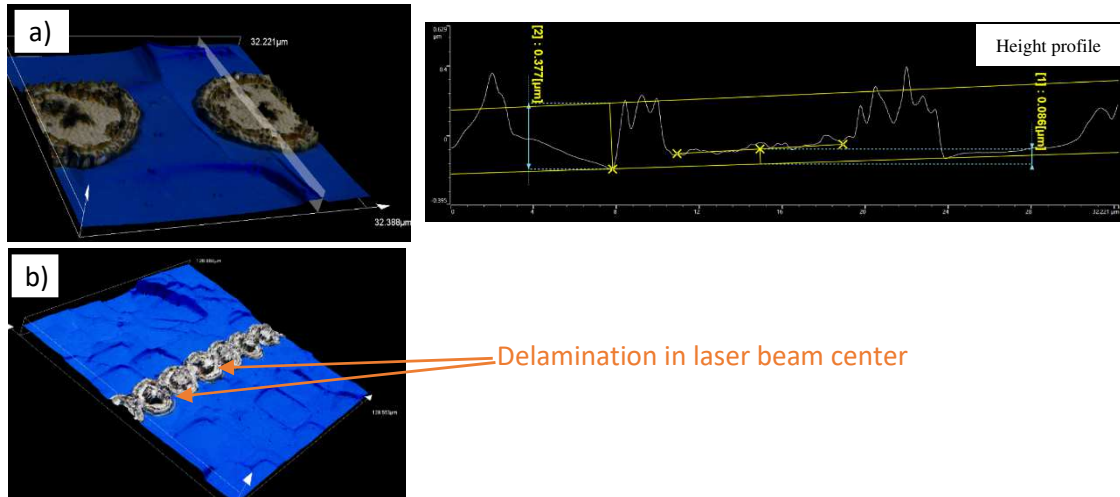


**Fig. 19.** CLSM images after nickel electroless deposition illustrating border effect and delamination in spot center at high fluence a)  $F_{\text{peak}}$  of  $0.505 \text{ J/cm}^2$ ,  $d = 24 \text{ μm}$  b)  $F_{\text{peak}}$  of  $0.896 \text{ J/cm}^2$ ,  $d = 32 \text{ μm}$ .

#### 4. Conclusion

In this paper, we have investigated laser contact opening on n-PERT precursors, composed of a  $\text{SiO}_x/\text{SiO}_x\text{N}_y$  stack on the rear polished side and  $\text{SiO}_x\text{N}_y$  layer on the front textured side, using a UV-ps laser. Various combination of laser parameters (fluence and overlapping) have been tested in order to understand ablation mechanisms and choose the optimized parameters limiting laser induced damages.

CLSM and SEM characterizations realized on laser impacts at the rear polished side have revealed ablated surfaces constituted in four different rather concentric areas, linked to the laser fluence spatial distribution impacted areas. LIPSS (LASER-induced periodic surface structures) were mainly observed in overlapped spot regions. On the front textured side,  $\text{SiO}_x\text{N}_y$  layer residues are visible on pyramids due to preferential ablation on edges, base and top of pyramids. LIPSS were clearly observed on pyramids, leading to a rougher surface. When spot overlapping is used, pyramids start to melt especially with high fluence. Fluence threshold has been determined to be in the range of around  $0.32 \text{ J/cm}^2$  for both sides (with a slightly lower value for the front side) and lower fluence require spot overlapping about 50% to perform satisfying laser contact opening. Heat Affected Zone visible on both sides is attributed to amorphous silicon formation and disappears after a post-laser annealing at  $750^\circ\text{C}$ .

Bulk and surface compositions were investigated by EDS and XPS analysis to obtain more information about the fine chemistry after LASER opening. Results on double impacted surfaces suggest that silicon oxide has been generated by the laser process, which confirms the higher thermal impact induced by spot overlapping. Indeed, laser heating effect could enhance the silicon reactivity toward oxygen leading to oxide phase formation. However, we cannot attest a complete ablation of the  $\text{SiO}_x\text{N}_y/\text{SiO}_x$  initial stack and possible presence of initial silicon oxide layer trace. The XPS Si substrate signal brings information about the atomic arrangement and shows that silicon crystallinity is modified on both sides after laser ablation, whose main probable origin is the interaction with laser leading to an amorphization. XPS analysis after PLA suggests a partially re-crystallization of a-Si on the rear side which is consistent with disappearance of light blue area observed by CLSM.

Based on these results and material properties, we have suggested an ablation mechanism relying on partial lift off for both sides.

Four probe measurements after laser ablation displayed that  $R_{sq}$  initial values are preserved on both sides, even for high fluence values, provided that overlapping was not used. In contrast,  $R_{sq}$  increases with overlapping and this is especially the case for the front textured side where laser impact is enhanced due to diffusion on pyramids and where p+/n junction can be destroyed. Increase of  $R_{sq}$  with overlapping is much more important on the front textured side than on the rear polished one. It is thus preferable to not use spot overlapping especially on the front side. However, overlapping, with fluence below fluence threshold, is necessary to obtain satisfying laser contact opening and laser impact on  $R_{sq}$  can be neglected for both sides. These conditions enable to increase roughness on the rear polished side and limit dielectric layers residues on the front textured side. A post laser annealing is also beneficial for electrical properties through reduction of silicon square resistance.

PL-QSS PC measurements suggest an important laser impact on carrier lifetime, for both sides, for fluence  $\geq 1.75$  J/cm<sup>2</sup> even without overlapping. This is probably due to defects generation in silicon underlying. We have also demonstrated that carrier lifetime was reduced due to a-Si formation. The importance of a-Si recrystallization is again illustrated by the improvement of carrier lifetime after PLA. Moreover, we demonstrated that HF cannot etch SiO<sub>x</sub> and a-Si below heat-impacted zones (light blue areas) leading to lower carrier lifetime when high proportion of HAZ is present. Before PL-QSS PC analysis, we could thus think that a solution to limit laser impact would be to slightly space out laser spot but this is actually not recommended.

Finally, optimized laser parameters proposed are as following:

- Conditions n°1:  $F_p$  is just above  $F_{th}$  and opened areas are just in contact along a line but also from one line to another which corresponds to 0.32 J/cm<sup>2</sup> -  $d = 10$   $\mu$ m for the both sides. When opened area do not overlap, we can reasonably use fluence up to 0.7 J/cm<sup>2</sup> without increasing significantly laser impact.
- Conditions n°2:  $F_p < F_{th}$  and 50 % overlapping of opened areas is used. That corresponds to 0.24 J/cm<sup>2</sup> and  $d = 7$   $\mu$ m for the both sides.

After selective laser opening, palladium activation and Ni electroless deposition have been realized. Ablation mechanism suggested is in good agreement with morphology of Pd deposits observed. Consequently, it appears that non-homogenous surface morphology and composition after laser ablation lead to non-homogeneous metallization and adherence issues on the rear polished side.

This work will be complete with SIMS (Secondary Ionization Mass Spectrometry) and ECV (Electrochemical capacitance-voltage) measurements to investigated laser impact on doping profile. Nano-Auger analyses will be performed to obtain chemical information at a local scale and bring separate chemical information of the areas n°1, 2 and 2<sub>bis</sub> observed on the rear side. Finally, the study of laser parameter impact on the quality of Ni/Cu plated contacts will be pursue in particular through contact resistance measurements and I-V analysis.

## Acknowledgements

This work was carried out in the framework of project A of IPVF (Institut Photovoltaïque d'Ile-de-France) and has been supported by the French Government in the frame of the program of investment for the future

(Programme d'Investissement d'Avenir - ANR-IEED-002-01). Authors would like to thanks ISC Konstanz for providing n-PERT silicon solar cells precursors.

## References

- [1] ITRPV Roadmap 2019 - Tenth edition - 2018 results. <https://itrpv.vdma.org/> (accessed February 7, 2019).
- [2] BP Statistical Review of World Energy - Main Indicators - knoema.com, Knoema. (n.d.). <https://knoema.fr//BPWES2017/bp-statistical-review-of-world-energy-main-indicators> (accessed November 18, 2018).
- [3] Imprint, A. us, T. and Conditions, P. and C. Policy, Market Survey on Screen Printers 2018 | TaiyangNews, (n.d.). <http://taiyangnews.info/reports/market-survey-on-screen-printers-2018/> (accessed October 24, 2018).
- [4] B. Gerdes, M. Jehle, N. Lass, L. Riegger, A. Spribille, M. Linse, F. Clement, R. Zengerle, P. Koltay, Front side metallization of silicon solar cells by direct printing of molten metal, *Solar Energy Materials and Solar Cells*. 180 (2018) 83–90. doi:10.1016/j.solmat.2018.02.022.
- [5] L. Kuang-Chieh, L. Yueh-Lin, L. Ming-Shiou, C. Chia-Chih, L. Chi-Chun, W. Chien-Chun, Cu-plated electrodes with laser contact opening on n-type crystalline silicon solar cells, Motech Industries, Inc, Tainan, Taiwan., n.d. <https://www.pv-tech.org/technical-papers/cu-plated-electrodes-with-laser-contact-opening-on-n-type-crystalline-silic> (accessed February 4, 2019).
- [6] M. Gebhardt, T. Kießling, M. Grimm, Laser Contact Opening of High Efficient Solar Cells: On the fly laser processing of PERC solar cells, *LTJ*. 11 (2014) 18–20. doi:10.1002/latj.201400016.
- [7] M.S. Trtica, B.M. Gakovic, B.B. Radak, D. Batani, T. Desai, M. Bussoli, Periodic surface structures on crystalline silicon created by 532nm picosecond Nd:YAG laser pulses, *Applied Surface Science*. 254 (2007) 1377–1381. doi:10.1016/j.apsusc.2007.06.050.
- [8] M. Kim, D. Kim, D. Kim, Y. Kang, Analysis of laser-induced damage during laser ablation process using picosecond pulse width laser to fabricate highly efficient PERC cells, *Solar Energy*. 108 (2014) 101–106. doi:10.1016/j.solener.2014.06.020.
- [9] C. Dang, R. Labie, L. Tous, R. Russell, M. Recaman, J. Deckers, A. Uruena, F. Duerinckx, J. Poortmans, Investigation of Laser Ablation Induced Defects in Crystalline Silicon Solar Cells, *Energy Procedia*. 55 (2014) 649–655. doi:10.1016/j.egypro.2014.08.040.
- [10] G. Heinrich, A. Lawerenz, Non-linear absorption of femtosecond laser pulses in a SiNx layer - Influence of silicon doping type, *Solar Energy Materials and Solar Cells*. 120 (2014) 317–322. doi:10.1016/j.solmat.2013.05.004.
- [11] G. Heinrich, M. Bähr, K. Stolberg, T. Wütherich, M. Leonhardt, A. Lawerenz, Investigation of ablation mechanisms for selective laser ablation of silicon nitride layers, *Energy Procedia*. 8 (2011) 592–597. doi:10.1016/j.egypro.2011.06.188.
- [12] G. Poulain, Procédés laser pour la réalisation de cellules photovoltaïques en silicium à haut rendement, Lyon, INSA, 2012. <http://www.theses.fr/2012ISAL0099> (accessed November 20, 2017).
- [13] A. Frey, J. Engelhardt, G. Micard, G. Hahn, B. Terheiden, Investigation of fill factor losses on 20.2% efficient n-type mono-like silicon solar cells with laser contact opening, *Physica Status Solidi (RRL) - Rapid Research Letters*. 10 (2016) 143–147. doi:10.1002/pssr.201510334.
- [14] Z. Du, N. Palina, J. Chen, M. Hong, B. Hoex, Rear-Side Contact Opening by Laser Ablation for Industrial Screen-Printed Aluminium Local Back Surface Field Silicon Wafer Solar Cells, *Energy Procedia*. 25 (2012) 19–27. doi:10.1016/j.egypro.2012.07.003.
- [15] A. Buechler, S. Kluska, F. Meyer, A. Brand, G. Cimiotti, J. Bartsch, M. Glatthaar, Interface oxides in femtosecond laser structured plated Ni-Cu-Ag contacts for silicon solar cells, *Solar Energy Materials and Solar Cells*. 166 (2017) 197–203. doi:10.1016/j.solmat.2017.03.016.
- [16] G. Heinrich, I. Hšger, M. Bšhr, K. Stolberg, T. WŸtherich, M. Leonhardt, A. Lawerenz, G. Gobsch, Investigation of Laser Irradiated Areas with Electron Backscatter Diffraction, *Energy Procedia*. 27 (2012) 491–496. doi:10.1016/j.egypro.2012.07.099.
- [17] A. Lennon, J. Colwell, K.P. Rodbell, Challenges facing copper-plated metallisation for silicon photovoltaics: Insights from integrated circuit technology development, *Prog Photovolt Res Appl*. 27 (2019) 67–97. doi:10.1002/pip.3062.
- [18] C. Dang, R. Labie, E. Simoen, J. Poortmans, Detailed structural and electrical characterization of plated crystalline silicon solar cells, *Solar Energy Materials and Solar Cells*. 184 (2018) 57–66. doi:10.1016/j.solmat.2018.04.016.
- [19] B.N. Chichkov, C. Momma, S. Nolte, F. von Alvensleben, A. Tünnermann, Femtosecond, picosecond and nanosecond laser ablation of solids, *Applied Physics A: Materials Science & Processing*. 63 (1996) 109–115. doi:10.1007/BF01567637.

- [20] J. Bonse, S. Baudach, J. Krüger, W. Kautek, M. Lenzner, Femtosecond laser ablation of silicon–modification thresholds and morphology, *Applied Physics A*. 74 (2002) 19–25. doi:10.1007/s003390100893.
- [21] J. Siegel, Structural transformation dynamics in Ge films upon ultrashort laser pulse irradiation, Universidad Autonoma de Madrid, 1998. <http://hdl.handle.net/10486/674668>.
- [22] M. Schulz-Ruhtenberg, D. Trusheim, J. Das, S. Krantz, J. Wieduwilt, Influence of Pulse Duration in Picosecond Laser Ablation of Silicon Nitride Layers, *Energy Procedia*. 8 (2011) 614–619. doi:10.1016/j.egypro.2011.06.191.
- [23] J. Thorstensen, S.E. Foss, Investigation of Depth of Laser Damage to Silicon as Function of Wavelength and Pulse Duration, *Energy Procedia*. 38 (2013) 794–800. doi:10.1016/j.egypro.2013.07.348.
- [24] S. Binetti, A. Le Donne, A. Rolfi, B. Jäggi, B. Neuenschwander, C. Busto, C. Frigeri, D. Scorticati, L. Longoni, S. Pellegrino, Picosecond laser texturization of mc-silicon for photovoltaics: A comparison between 1064 nm, 532 nm and 355 nm radiation wavelengths, *Applied Surface Science*. 371 (2016) 196–202. doi:10.1016/j.apsusc.2016.02.187.
- [25] N. Bay, A.A. Brand, A. Büchler, J. Burschik, S. Kluska, H.H. Kuehnlein, M. Passig, D. Pysch, M. Sieber, Benefits of different process routes for industrial direct front side plating, *Energy Procedia*. 124 (2017) 823–828. doi:10.1016/j.egypro.2017.09.353.
- [26] L. Chahed, M.L. Thèye, B. Bourdon, Effets du recuit sur les propriétés optiques du silicium amorphe hydrogéné, *Journal de Physique*. 44 (1983) 387–392. doi:10.1051/jphys:01983004403038700.
- [27] J.F. Moulder, *Handbook of XRay Photoelectron Spectroscopy*, 1992. <https://fr.scribd.com/document/311527850/John-F-Moulder-PHI-Handbook-of-XRay-Photoelectron-Spectroscopy> (accessed January 10, 2019).
- [28] J.-W. He, X. Xu, J.S. Corneille, D.W. Goodman, X-ray photoelectron spectroscopic characterization of ultra-thin silicon oxide films on a Mo(100) surface, *Surface Science*. 279 (1992) 119–126. doi:10.1016/0039-6028(92)90748-U.
- [29] J.R. Shallenberger, D.A. Cole, S.W. Novak, Characterization of silicon oxynitride thin films by x-ray photoelectron spectroscopy, *Journal of Vacuum Science & Technology A*. 17 (1999) 1086–1090. doi:10.1116/1.582038.
- [30] E. Dehan, P. Temple-Boyer, R. Henda, J.J. Pedroviejo, E. Scheid, Optical and structural properties of SiO<sub>x</sub> and SiN<sub>x</sub> materials, *Thin Solid Films*. 266 (1995) 14–19. doi:10.1016/0040-6090(95)06635-7.
- [31] J. J. Low, M. L. Kreider, D. P. Pulsifer, A. S. Jones, T. Gilani, Band Gap Energy in Silicon, *American Journal of Undergraduate Research*. 7 (2008). doi:10.33697/ajur.2008.010.
- [32] X.Y. Chen, Y.F. Lu, L.J. Tang, Y.H. Wu, B.J. Cho, X.J. Xu, J.R. Dong, W.D. Song, Annealing and oxidation of silicon oxide films prepared by plasma-enhanced chemical vapor deposition, *Journal of Applied Physics*. 97 (2004) 014913. doi:10.1063/1.1829789.
- [33] T. Schutz-Kuchly, A. Slaoui, J. Zelgowski, A. Bahouka, M. Pawlik, J.-P. Vilcot, E. Delbos, M. Bouttemy, R. Cabal, UV and IR laser induced ablation of Al<sub>2</sub>O<sub>3</sub>/SiN:H and a-Si:H/SiN:H, *EPJ Photovolt*. 5 (2014) 55201. doi:10.1051/epjpv/2013027.
- [34] A. Knorz, M. Peters, A. Grohe, C. Harmel, R. Preu, Selective laser ablation of SiN<sub>x</sub> layers on textured surfaces for low temperature front side metallizations, *Progress in Photovoltaics: Research and Applications*. 17 (2009) 127–136. doi:10.1002/pip.856.
- [35] Y.-J. Oh, S.M. Cho, C.-H. Chung, An In Situ ATR-FTIR Study on Palladium Displacement Reaction on Hydrogen-Terminated Silicon Surface, *J. Electrochem. Soc.* 152 (2005) C348. doi:10.1149/1.1896326.
- [36] H.E. Belghiti, D. Aureau, M. Bouttemy, E. Delbos, A. Etcheberry, Impact of the Silicon Substrates and Activation in the Nickel Electroless Plating, *ECS Trans.* 50 (2013) 17–24. doi:10.1149/05053.0017ecst.
- [37] M. Schlesinger, Electroless Deposition of Nickel, in: *Modern Electroplating*, John Wiley & Sons, Ltd, 2011: pp. 447–458. doi:10.1002/9780470602638.ch18.